

GT2009-59619

NUMERICAL COMPUTATION OF THE PULSATILE FLOW IN A TURBOCHARGER WITH REALISTIC INFLOW CONDITIONS FROM AN EXHAUST MANIFOLD

Fredrik Hellstrom*

Industrial PhD student, GM Powertrain, Sweden
Department of Mechanics
The Royal Institute of Technology
SE-100 44 Stockholm
Sweden
Email: fredrik.hellstrom@mech.kth.se

Laszlo Fuchs

KTH CICERO, Department of Mechanics
The Royal Institute of Technology
SE-100 44 Stockholm
Sweden
Email: lf@mech.kth.se

ABSTRACT

The combined effect of different secondary perturbations at the turbine inlet and the pulsatile flow on the turbine performance was assessed and quantified by using Large Eddy Simulation. The geometrical configuration consists of a 4-1 exhaust manifold and a radial turbine. At the inlet to each port of the manifold, engine realistic pulsatile mass flow and temperature fields are specified. The turbine used in this numerical study is a vaneless radial turbine with 9 blades, with a size that is typical for a turbocharger mounted on a 2.0 liters IC engine of passenger cars.

The flow field is investigated and the generated vortices are visualized to enable a better insight into the unsteady flow field. Correlations between the turbine inflow conditions, such as mass flow rate, strength of secondary flow components, and the turbine performance have also been studied. The results show that the flow field entering the turbine is heavily disturbed with strong secondary flow components and disturbed axial velocity profile. Between the inlet to the turbine and the wheel, the strength of the

secondary flow and the level of the disturbances of the axial flow decrease which gives large losses in this region. Even though the magnitude of the disturbances decrease, the flow entering the wheel will still be disturbed, resulting in a perturb inlet flow to the wheel which affects the shaft power output from the turbine.

NOMENCLATURE

p Pressure (Pa)
 T Temperature (K)
 ρ Density (kg/m^3)
 u_i Velocity components (m/s)
 U, V, W Velocity components (m/s)
 μ Dynamic viscosity (Ns/m^2)
 h Specific enthalpy (J/kg)
 \dot{m} Mass flow rate (kg/s)
 q_i Heat flux (W/m^2)
 C_p Specific heat at constant pressure (J/kg K)
 γ Ratio of specific heat $\gamma=C_p/(C_p-R)$
 R Gas constant (287 J/kg K)

*Address all correspondence to this author.

t Time (s)
 x_i Cartesian coordinates (m)
 ω Angular velocity (rad/s)
 P Power (W)
 M Torque (Nm)
 η Efficiency
 Sw Secondary flow index
 IU Uniformity index

₁ Turbine inlet
₂ Turbine outlet
₀ Stagnation

INTRODUCTION

One way to reduce fuel consumption and emissions is to downsize the engine in combination with turbo-charging whereby one can increase the density of the air that is admitted to the cylinders. Turbochargers, which consist of a turbine part and a compressor part utilize the hot exhaust gases as energy source and thereby enhancing also the total efficiency of the engine. This means that the wasted energy in the exhaust gas, which can be as much as 30–40 percents of the chemical energy released by the combustion, is used to drive the compressor. The turbine works under highly unsteady flow conditions, since the exhaust flow is pulsatile and turbulent and with a varying strength of the axial and secondary flow components.

The effects of pulsatile flow on the turbine performance have been investigated with both experimental and numerical methods. For turbines operating under pulsatile flow conditions, the mean efficiency is lower as compared to non-pulsatile flow conditions for the same mass flow and pressure ratio. The instantaneous performance can be higher or lower, see for example [1], [2], [3] and [4]. It has to be emphasized that it may be difficult to compute the isentropic efficiency in an accurate way, due to the phase shift between pressure and mass flow and the time it takes for the energy to propagate from the measuring point to the turbine wheel [5]. It is equally difficult to measure the time dependent shaft power which, for example, makes direct model validation problematic.

Winterbone et al. [2] investigated the performance of a radial turbine under both non-pulsatile and pulsatile flow conditions. The frequency of the pulsatile flow was 35 Hz. To measure the time dependent shaft power, they used a hydraulic dynamometer in combination with the knowledge of the varying angular velocity. By analyzing the measured pressure distribution around the volute for both non-pulsatile and pulsatile operating conditions, they concluded that the flow in the turbine volute can be treated as being quasi-stationary, since the rate of change of pressure with respect to distance was much greater than it was with respect to time. The shaft torque measurements were time-resolved, and

therefore they could compare that data to the time resolved pressure traces at the inlet and also the phase lag between the pressure trace and the torque trace. This lag was found to be about 40° . The time this phase lag corresponds to, is larger than the pressure wave travel time from the inlet to the rotor, and hence the phase lag cannot only be attributed to the wave propagation time. Winterbone et al. also reported that the mass flow pulses were approximately in phase with the pressure pulses, but the mass flow trace was quite noisy, so it was difficult to determine any phase shift. The rotational speed of the wheel varied by approximately 2% during the pulse. Wallace et al. [6] investigated the effects of different frequencies, mass flows and turbine speeds. They used a dynamometer to measure the shaft torque of the turbine, and this dynamometer could be operated up to 100 000 rpm. The frequency of the pulsatile flow was varied from 16.7 Hz to 50 Hz, and they concluded that the turbine shaft torque first increased and then decreased with increasing frequency. The shaft power reduced slightly with increasing mass flow for constant rotational speed of the turbine wheel and mean inlet pressure to the turbine. Benson and Scrimshaw [7] conducted experiments where the pulse frequency was varied from 30 Hz to 70 Hz, and the rotational speed of the turbine wheel was varied from 30 000 rpm to 60 000 rpm. The used turbine was a nozzleed radial turbine with twin entries. The results showed also that the efficiency increased up to a pulse frequency of 60 Hz, and then decreased with further increase in pulse frequency.

Dale and Watson [3] measured the shaft power of a twin entry turbine working in pulsatile flow. They concluded that the efficiency varied with varying admissions in the two entries, where the lowest efficiency occurred when the flow entered only one of the two entries. For an operation point with a pulse frequency of 40 Hz, the maximum deviation of the instantaneous efficiency from the quasi-stationary assumption was up to 10%, with both higher and lower values than the efficiency from the quasi-stationary assumption. Karamanis et al. [8] concluded from an experimental study, that the deviation of isentropic efficiency from the quasi-stationary assumption was reduced as the pulse frequency was increased for a mixed flow turbine. The frequency of the pulsatile flow was 40 Hz and 60 Hz, respectively. When they computed the isentropic efficiency, they applied a correction for the phase lag, which corresponded to the sonic travel time from the inlet to the wheel. The cycle-averaged efficiency was lower than the corresponding steady-state efficiency, due to the large variation of flow conditions. The incidence angle varied from -80° to 40° during the pulse. These results are in contradiction from conclusions reported by Hellstrom and Fuchs [5], who performed time resolved 3-D numerical computations of the flow in a radial turbine. Hellstrom and Fuchs considered three different pulsatile inflow conditions with different amplitude and frequency, and they concluded that the deviation from the quasi-stationary behavior increased with increasing frequency of the pulsations. They also showed that there exists a phase shift be-

tween the mass flow, pressure and shaft torque, which was not constant over the mass flow pulse. The phase shift also varied for different frequencies of the mass flow pulse. When plotting the mass flow versus the shaft torque, the trace forms a closed envelope depending on the phase shift and that the flow separates from the blade during the acceleration phase of the mass flow pulse.

In the experiment conducted by Arcoumanis et al. [9] the steady and unsteady performance of a mixed flow turbine was investigated for different rotational speeds of the wheel and with pulse frequencies of 40 Hz and 60 Hz. The results showed that the cycle averaged isentropic efficiencies were higher for a mixed flow turbine compared to a radial turbine. By using a cycle averaged efficiency, no phase shifting of the shaft torque is needed, which is beneficial, since the time-resolved isentropic efficiency is strongly affected by the size of the phase shift.

Lam et al. [10] performed a time resolved 3-dimensional numerical study of the pulsatile flow in a radial nozzleed turbine. They used the frozen rotor technique to model the rotation of the wheel. The results showed that instantaneous performance of the rotor under pulsatile conditions did not vary significantly from the non-pulsatile conditions, and Lam et al. concluded that the wheel can be treated as a quasi-steady device, while the volute must be treated as a non quasi-stationary flow device. Palfreyman and Martinez-Botas [11] investigated the pulsatile flow in a mixed flow turbocharger with numerical methods. They used a medium sized mixed flow nozzle-less turbine. They concluded that the used method with explicit rotation of the wheel, better captures the non quasi-stationary behavior of the turbine than the method used by Lam et al. [10]. But, this might also be an affect of that Palfreyman and Martinez-Botas used a nozzle-less turbine, without the damping the nozzles can introduce, leading to a more uniform flow into the rotor. At the inlet to the rotor, the incidence angle varied from -92° to $+60^\circ$, which gives raise to losses, due to strong tip vortices at the leading edge of the blades. The blade torque and the work output fluctuated substantially and with the frequency of the pulse. A perturbation with same frequency as the blade passage frequency was also superimposed on the shaft torque trace, which is an effect of the blades passing the tongue. The velocity field within the turbine wheel also varied substantially during the pulse due to poor flow guidance at the entrance to the turbine wheel. The trajectory of the mass flow versus efficiency showed a hysteresis loop, which encapsulates the quasi-steady values. This is, according to Palfreyman and Martinez-Botas, due to the imbalance between inlet and outlet mass flow during the pulse and the “filling and emptying” of the volute as the turbine acts as a restriction. They also reported a phase lag between the computed isentropic work and the actual work.

In addition to effects of the pulsatile flow (driven by the engine cycles) there is also a cross-sectional motion added to the axial flow velocity component at the inlet to the turbine. This

secondary motion may consist of swirl, Dean vortices and other non-axial velocity components which is formed in the exhaust manifold ([12], [13], [14], and [15]). The strength and the direction of the vortices vary in time depending on the pulsatile flow, the firing sequence of the engine and the geometry of the manifold. The rate of decay for these secondary flows is very low [16], especially for these kinds of geometries, where the distance between the bends in the manifold and the turbine is often less than a few pipe diameters. The turbulence intensity varies also during the cycle, since the Reynolds number varies during the cycle. In a previous investigation by Hellstrom and Fuchs [17], they showed with a numerical study that the output shaft power differs up to 20% with and without secondary flow perturbations at the inlet for a constant mass flow.

Previous investigations have focused on geometrical effects, numerical modeling considerations, effects of the engine frequency and flow amplitude, and effects of secondary flow for non-pulsatile flow and have not taken effects of the combination of pulsatile-flow with secondary flow effects into consideration. Therefore, the effect such perturbations on the turbine performance is assessed and quantified by performing a numerical study with Large Eddy Simulation of a geometrical configuration consisting of an exhaust manifold and a nine-bladed radial vaneless turbine. The size of the geometry is typical for an exhaust manifold and turbocharger mounted on a 2.0 liters IC engine of a passenger car. The flow field for the cases is also investigated and the vortex cores are visualized to enable a better insight into the unsteady flow field.

1 NUMERICAL METHODS

The governing equations that describe the conservation of mass (1), momentum (2) and energy (3) are the Navier-Stokes (NS) equations and the energy equation complemented with the equation of state (4):

$$\frac{\partial \rho}{\partial t} + \frac{\partial}{\partial x_j} (\rho u_j) = 0 \quad (1)$$

$$\frac{\partial}{\partial t} (\rho \cdot u_i) + \frac{\partial}{\partial x_j} (\rho u_i u_j) = -\frac{\partial p}{\partial x_i} + \frac{\partial \tau_{ij}}{\partial x_j} \quad (2)$$

$$\frac{\partial}{\partial t} (\rho \cdot h) + \frac{\partial}{\partial x_j} (\rho u_j \cdot h) = \frac{\partial p}{\partial t} + u_j \frac{\partial p}{\partial x_j} + \tau_{ij} \frac{\partial u_i}{\partial x_j} - \frac{\partial q_j}{\partial x_j} \quad (3)$$

$$p = \rho TR \quad (4)$$

where τ_{ij} is the stress tensor, defined as:

$$\tau_{ij} = \mu \left(\frac{\partial u_i}{\partial x_j} + \frac{\partial u_j}{\partial x_i} - \frac{2}{3} \delta_{ij} \frac{\partial u_k}{\partial x_k} \right) \quad (5)$$

Since the flow studied here is turbulent and highly unsteady, with both local unsteady flow structures and global pulsatile mass flow, the turbulence of the flow has been handled by Large Eddy Simulation (LES). The objective of LES is to explicitly compute the large scales of the turbulence, while modeling the effects of the unresolved scales. A major role of the smallest scales is to dissipate the turbulent energy that is transferred (in the average sense) from the larger scales to the smaller ones through the so-called energy cascade. By resolving the temporal and spatial behavior of the large scales one can capture and separate coherent structures from the random turbulence eddies. Such information that cannot be obtained by the Reynolds Averaged Navier-Stokes modeling (RANS) approach is important in many applications, for example where large scale structures play important. The scale separation (to resolved and unresolved scales) is achieved by spatial filtering of the governing equations, where the filter width is a function of the cell size.

In order to avoid the need for subgrid scale modeling in the continuity equation, the density averaging is introduced:

$$\tilde{\Theta} = \overline{\rho\Theta} / \bar{\rho} \quad (6)$$

The filtered NS-equations (1), (2) are:

$$\frac{\partial \bar{\rho}}{\partial t} + \frac{\partial}{\partial x_j} (\bar{\rho} \tilde{u}_j) = 0 \quad (7)$$

$$\frac{\partial}{\partial t} (\bar{\rho} \tilde{u}_i) + \frac{\partial}{\partial x_j} (\bar{\rho} \tilde{u}_i \tilde{u}_j) = - \frac{\partial \bar{p}}{\partial x_i} + \frac{\partial \tilde{\tau}_{ij}}{\partial x_j} + \frac{\partial \tau_{SGSij}}{\partial x_j} \quad (8)$$

where τ_{SGSij} is the subgrid stress tensor that has to be modeled. This term can be modeled in different ways, for example by the Smagorinsky model where the effects of the unresolved scales of the turbulence on the resolved scales are modeled as an increase of the viscosity. Many of the SGS-models, such as the Smagorinsky model are known to be too diffusive, especially on relative course meshes. In this study an Implicit LES approach has been used, which implies that no explicit subgrid scale model is explicitly added to the filtered NS-equations; i.e. $\tau_{SGSij}=0$. Instead, only the numerical dissipation accounts for the subgrid scale dissipation at the smallest scales.

The filtered governing equations are discretized by a finite volume method. For the temporal discretization a first order Euler implicit scheme has been used. As long as the time step is small enough the accuracy of the numerical results is determined by the order of the spatial discretization scheme. Since the grid resolution is high, in order to resolve the relevant fluctuations, one has also use correspondingly small time-steps with Courant number smaller than unity for consistency with the physics of the flow. A formally second order Monotone Advection and Reconstruction Scheme (MARS) has been used for spatial discretization of the convective terms. This scheme employs a total variation diminishing (TVD) scheme, making it particularly well suited to capture the strong gradients as such are expected for these cases. For the viscous terms, a blended central difference scheme has been used. A modified version of the PISO solver has been used to solve the equations at each time-step, where the number of corrector stages is determined by a convergence criteria. Each time step is assumed to be converged when the residuals of the parameters are reduced by about two orders of magnitude from their initial value. Since the time-steps are small such a reduction implies a high degree of convergence in each time-step and the residuals are of the same order as the round off error. The turbine wheel has been modeled with the sliding mesh technique, which implies that the rotor is described by a grid that rotates relative to the grid that is used to describe the turbine house. At the interface between the moving and the stationary part, the moving mesh is made to slide past the stationary part. At the sliding interface, the connectivity for cells on either side of the interface changes at each time step. This is implemented in a way that there are no restrictions on the relative position of the cell faces on either side of the sliding interface, i.e. cell faces across the sliding interface do not to have a one-to-one correspondence. This also means that there are no circumferentially averaging over the interface between the wheel and the turbine, as it is in some rotating reference techniques, and the accuracy of the results gets better. In order to preserve flux continuity across the sliding interface and to avoid non-physical perturbations, the interpolation over the sliding interface must be done in appropriate way. Also, the used time step and the cell sizes on both side of sliding interface must not be too large. Too large cell sizes at parts of the sliding interface imply that solution is smeared out; for example when the leading edge of the wheel is passing a region with large cells on the other side of the sliding region. The rotational speed of the wheel and cell sizes at the sliding interface sets limitations on the time step; the time step must be small enough to ensure that cells on both sides of the sliding interface do not pass each other completely during one time step.

NUMERICAL ACCURACY

The numerical accuracy study is performed on a simplified turbine geometry, where the complete wheel and only parts of

the volute and the diffuser is modeled to reduce the computational time. The rotational speed for the rotor is 97 897 rpm and a fixed mass flow and temperature are specified at the inlet. At the outlet, a constant pressure is applied. The method (both modeling and numerical method) used in the numerical accuracy study is the same as in this study. The method used for the estimation of the uncertainty is the method proposed by Celik [18], which is based on grid refinements. The order of accuracy for the actual variable is calculated for the different refinement levels, and from the order of accuracy, the uncertainty of the results can be computed. For this accuracy study, the pressure drop over the simplified turbine and the shaft torque are evaluated. As can

Table 1. COMPUTATIONAL ACCURACY STUDY

| Grid number | Number of cells in the rotor | Averaged cell size (mm) | Shaft torque (Nm) | Pressure drop (kPa) |
|-------------|------------------------------|-------------------------|-------------------|---------------------|
| 1 | 76 662 | 0.65 | 0.362 | 30.90 |
| 2 | 297 648 | 0.42 | 0.276 | 30.28 |
| 3 | 541 008 | 0.34 | 0.287 | 29.86 |
| 4 | 968 229 | 0.28 | 0.290 | 29.83 |

be seen in Table 1, the convergence for grid number 2, 3, and 4 is monotone (better than first order), and the uncertainty for the shaft torque for the finest grid is about seven percent and for the pressure drop 0.3%. To perform a GCI study for the velocity field for time resolved unsteady flow is very computational expensive, since in this case with a rotating wheel, phase averaged data has to be used. Therefore, only integrated values are used in the grid convergence study. As can be seen in Table 1 and 2, the finest grid for the wheel used in the GCI-study is not used for the computations for the complete turbine due to the very long computation times. Therefore a computational grid with the same number of cells in the rotor-region as for grid 2 in the grid convergence study has been used in this study.

CASE SETUP

The geometry used in this case consists of 4-1 exhaust manifold and a radial turbine, see Figure 1. The turbine used in this study is a commercial available turbine with a size that is typical for a turbocharger mounted on a 2.0 liter IC engine of a passenger car. The turbine is a nozzle-less, 9 bladed radial turbine with the waste-gate valve closed. The complete geometrical configuration, turbine and the turbine wheel is shown in Figure 1. The

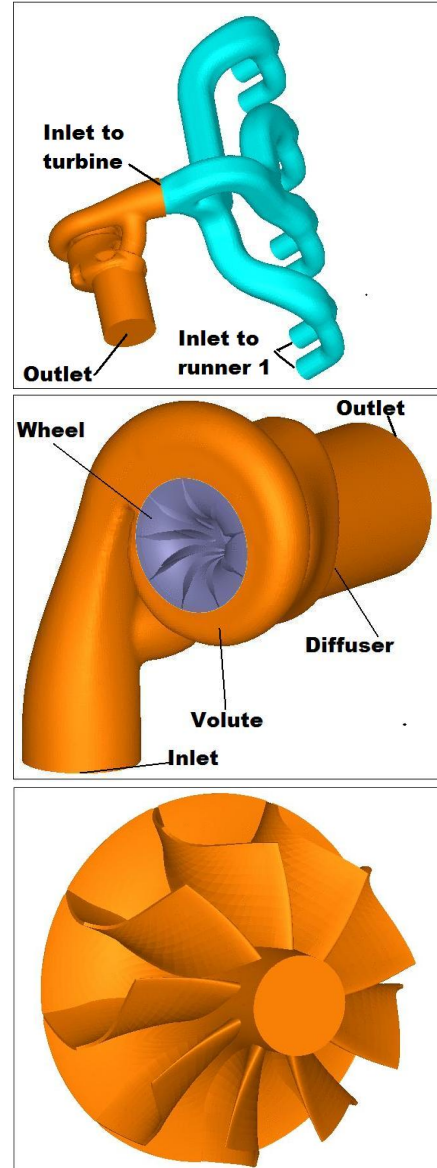


Figure 1. The complete assembly, turbine geometry and the wheel.

leading edge tip radius of the wheel is 22.10 mm and the trailing edge tip radius is 18.75 mm. The total number of cells for the mesh of the turbine are 1 111 720 and the number of cells for the mesh of the manifold are 212 732. The cell distribution is reported in Table 2. The grid resolution is good enough to capture the large energy carrying eddies, which also can be seen in the plot of the energy spectra in Figure 7, which have orders of magnitude of decay.

The computational model of the turbine and the grid for one blade passage are shown in Figure 2. In the wheel, only hexahedral cells are used, while in the rest of the domain a grid with

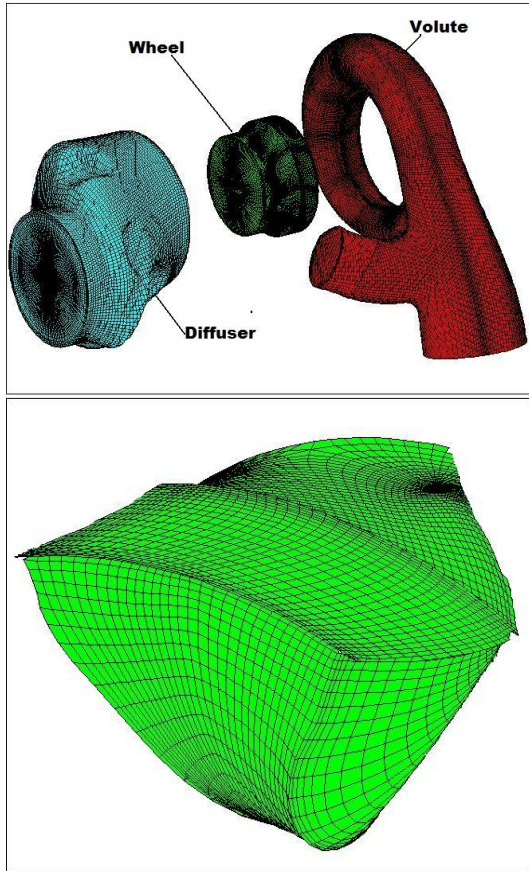


Figure 2. Numerical model of the different parts of the turbine and one blade passage.

dominantly hexahedral cells are used. The gap between the blade tips and shroud are resolved by 4 cells in the radial direction. The near-walls regions have better resolution than the regions in the “core-region”, but one should note that it is difficult to define the number of grid points in the “boundary layer”, since the thickness of that layer varies in space and time due to wakes and unsteady separation regions. To give some figures of the near-wall resolution, the maximum y^+ for the turbine housing is approximately 105, and the maximum y^+ for the region where the wheel is located is approximately 45. The concept of using y^+ is very appropriate on plane channel and boundary layer flows but one can discuss if it is relevant for not fully developed boundary layers such as those encountered in the turbocharger. The used time-step for the computations is $4 \cdot 10^{-7}$ seconds which corresponds to a rotation of the wheel of approximately $0.2^\circ/\text{time-step}$.

The mass flow and temperature at inlet to the exhaust manifold are taken from simulations from a one-dimensional IC engine simulation tool. In order to investigate the effect of perturbations at the inlet to turbine, the same mass flow and temperature field with a phase shift corresponding to the firing order of the

Table 2. Grid resolution in the different components

| | Number of cells |
|-------------------|-----------------|
| Manifold | 212 732 |
| Volute | 275 084 |
| Wheel | 297 648 |
| Diffuser | 538 988 |
| Complete assemble | 1 467 812 |

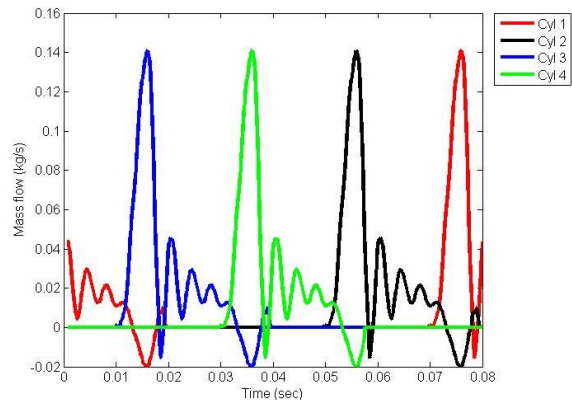


Figure 3. Mass flow at inlets to the manifold.

engine is applied at the inlet of the exhaust manifold. The frequency of the mass flow pulses and temperature corresponding to a engine working with wide open throttle at a speed of 1500 rpm, as shown in Figure 3 where the mass flow traces at the respectively inlet to the manifold are plotted. All walls are treated as being smooth and adiabatic, which is not the case for the real geometry. Both the manifold and the turbine housing will have a surface that is rough, but due to modeling techniques, the walls are assumed to be smooth. This will of course affect the performance of the turbine; Flaxington and Swain [19] estimates that the peak efficiency is typical 3 percents lower for a turbine with a caste house compared to a machined house. At the outlet, a non-reflecting boundary condition for the pressure is applied to avoid reflected pressure waves.

RESULTS

Since the mass flow and the pressure at both the inlet and outlet to the turbine is highly pulsatile, the shaft torque, and hence the shaft power varies in time, see Figure 4. As can be seen, the maximum shaft power for each mass flow pulse is not equal, despite the fact that the same mass flow and temperature

trace were applied at the inlet to the runners. This is the results of the fact that the different runners have different geometrical shapes, which create different inflow conditions to the turbine. The losses in the different runners also differ, since the lengths are not equal and the number of bends and the curvature radius of the bends differ for the different runners. The flow field in the manifold is not investigated here in detail and that component is included only to provide appropriate inflow conditions to the turbine. The focus here is on studying the flow field in the turbine itself.

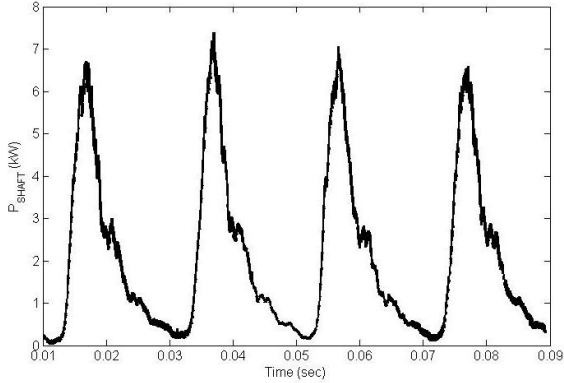


Figure 4. Shaft power during four pulses.

The shaft power P_S is defined as:

$$P_S = \bar{T}_{Shaft} \cdot \bar{\omega} \quad (9)$$

where the shaft torque, \bar{T}_{Shaft} is obtained by integrating the element forces due to the shear and pressure forces over the turbine wheel:

$$\bar{T}_{Shaft} = \int_S \bar{r} \times (\bar{f} \cdot \hat{n}) dS \quad (10)$$

The peak shaft power occurs when the mass flow comes from cylinder 4, which is the runner with the longest straight section. The second highest shaft power is obtained for runner 2, which compared to runners 1 and 3, has one bend less. The lowest shaft power is obtained for runner 1, which is the runner with sharpest bends. The deviation between the lowest and highest peak in shaft power is about 11%, while the difference between the peak of the inlet pressure is about 3% and mass flow is about 4%, respectively. Of course, the efficiency varies during the pulse, and since the phase shift between the mass flow, pressure and turbine shaft power is small, a time resolved isentropic

efficiency can be computed. The differences in the efficiency is small, see Figure 5 and the signal is quite noisy due to perturbations from blade passage effects on both the pressure signal at the turbine inlet and outlet and on the shaft power.

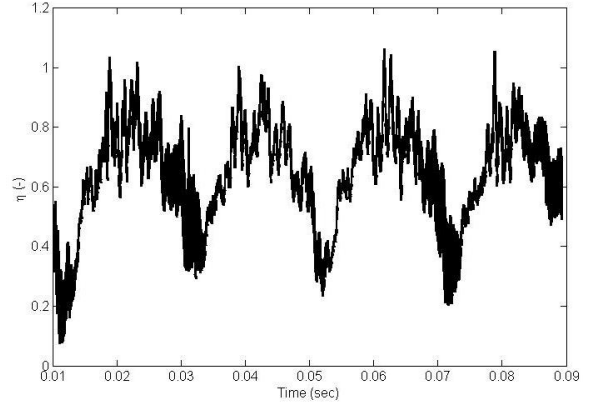


Figure 5. Instantaneous isentropic efficiency versus time.

The efficiency is defined as the ratio between the shaft power and the isentropic power:

$$\eta_{is} = \frac{P_S}{\dot{m} \cdot c_p \cdot T_{01} \cdot \left(1 - \frac{p_2}{p_{01}} \frac{\gamma-1}{\gamma}\right)} \quad (11)$$

p_{01} , T_{01} and \dot{m} is the total pressure, total temperature and mass flow at the inlet to the turbine and p_2 is the total pressure at the outlet of the turbine. The location of the inlet and outlet plane to the turbine can be seen in Figure 1. At the the turbine inlet plane and outlet plane, the respectively data used in for example the computations of the efficiency is the mass flux averaged data.

The amplitude of the mass flow pulses is damped in the volute, since is the manifold acts as a reservoir. There is also back flow into the cylinders before the exhaust valves close, which is an effect of the inlet boundary conditions from the one-dimensional IC engine simulation tool. For this operational point, there are at all times, mass flow into the turbine, but as can be seen in Figure 6, there is a substantial drop in mass flow when a peak is expected. When the flow accelerates in one of the runner and into the turbine, the flow reverses over the small tongue, which is located where runners 1 and 4 are connected to runners 2 and 3. The separated flow bubble is convected upstream into the other runner.

Due to the pulsatile inflow at each runner, the pressure in the different runners is varying, but almost in phase with each others. This implies that the flow going upwards in one runner is affected

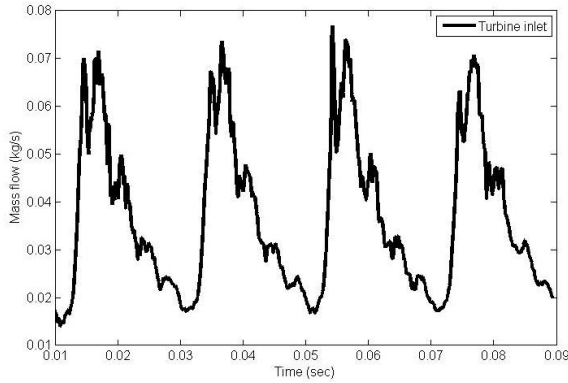


Figure 6. Mass flow at inlet to the turbine.

by the adverse pressure gradient, which leads to change in the main flow direction. Such changes in the flow are observed in the turbine. The drop in mass flow can be seen in the time resolved shaft power trace.

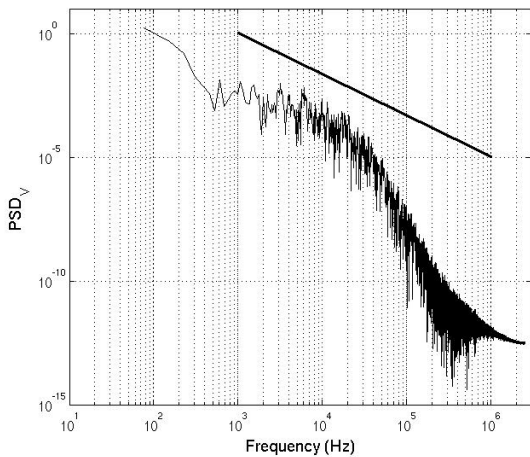


Figure 7. Power spectral density for stream wise velocity component for a position located one diameter downstream of the turbine inlet. The straight solid line shows the $-5/3$ slope. The cut-off frequency is $2.5 \cdot 10^6$ Hz.

The phase shift between the pressure and mass flow at the inlet to the turbine is varying during the pulse. The maximum phase shift, which occurs at the peaks of the mass flow into the turbine, is below 4° . This is less than a maximum phase shift of 20° which is reported by Hellstrom and Fuchs in [5]. In [5], a time varying mass flow and temperature trace were applied to the inlet to the same radial turbine as used in this study, but without any turbulence added. The rotational speed of the turbine wheel and the time mean mass flow over 4 pulses were the same as in this study. The flow into the turbine for the geometrical con-

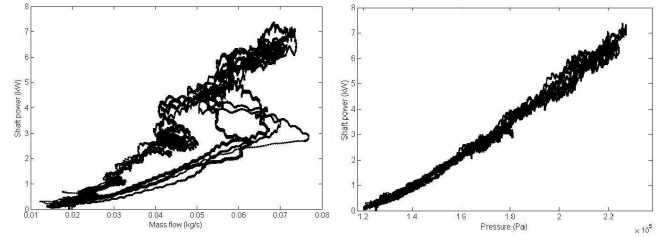


Figure 8. Shaft power plotted versus mass flow (right) and pressure (left) at turbine inlet, respectively

figuration used in this study is turbulent, which can be seen in Figure 7, where a spectra of the axial velocity component for a location two diameters downstream in the volute is plotted. As can be seen if the plot of the spectra, the range where the $-5/3$ slope is present is quite small. For pulsatile flow, the dissipation varies during the pulse, which also implies that the viscous length and time scales vary during the pulse. This will affect the high frequency part of spectra, while the low frequency part of the spectra is determined by large time (pulses) and length (geometrical) scales, and the range where the $-5/3$ slope is present will be smaller. The turbulence and inertia effects damp the phase lag between the pressure and the bulk flow, since for a pulsatile turbulent flow, the convection and the viscous terms in Navier-Stokes equations balance the pressure gradient term and the time derivative term. For a very low speed oscillating flow, the phase shift is 90° , where the pressure gradient term is balanced by the time derivative term. The phase shift between the bulk flow and the pressure implies that axial velocity profile is not a parabolic profile, which can be expected for a laminar pipe flow. Instead, the low momentum flow in the near wall regions is more sensitive to the axial pressure gradient than the bulk flow with high momentum resulting in higher axial velocity in the regions near the walls, see Figure 10. The non-uniform axial velocity distribution at the inlet to the turbine is also an effect of the bends situated upstream of the turbine. The small phase shift implies that the pressure, mass flow and shaft power is almost in phase. In Figure 8, the shaft power is plotted versus the mass flow and pressure respectively. As can be seen, the pressure and the shaft power are almost in phase, and from this point of view, the turbine can be treated as a quasi-stationary flow device. When plotting the mass flow versus the shaft power, one can see that the curve forms a closed envelope. The enclosed area for the operational point and geometrical configuration used in this study is smaller than the enclosed area for the corresponding case used in [5]. The phase shift, and hence the degree of quasi-stationary behavior of the turbine with respect to the mass flow, pressure and temperature at the inlet to the turbine, do not only depend on the frequency of the pulses, but also of the geometrical configuration upstream of the turbine.

The inflow conditions into the turbine affect the performance

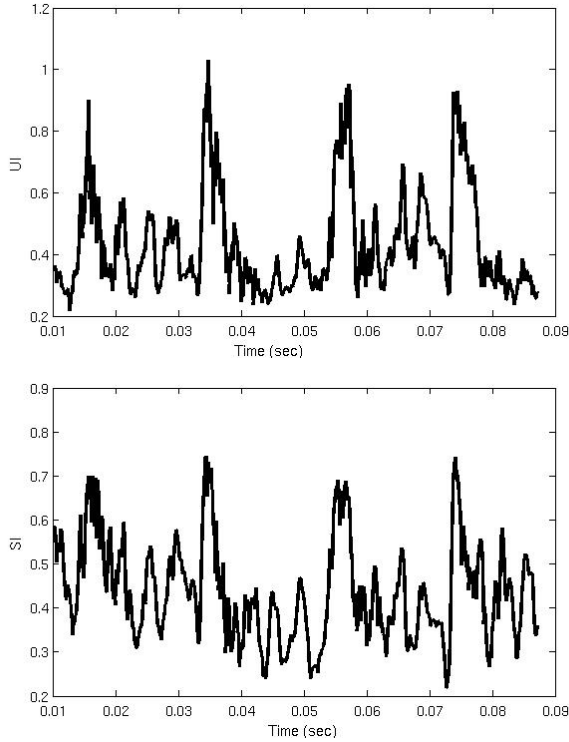


Figure 9. Velocity distribution at high mass flow rate. Upper figure: Uniformity index computed at the inlet plane to the turbine. Lower figure: Secondary flow index computed at the inlet plane to the turbine.

of the turbine. One way to give a measure of the level of the disturbances of the inflow conditions is to use two different dimensionless numbers, the secondary flow index and the uniformity index. The secondary flow index is here defined as:

$$Sw = \sum_i^n \sqrt{\frac{V_i^2 + W_i^2}{U_i^2 + V_i^2 + W_i^2}} / n \quad (12)$$

where V and W denote the in plane velocity components and the summation is taken over the whole plane. Sw is thus a measure for the strength of the in-plane kinetic energy as compared to the total kinetic energy of the fluid. Here, we apply this definition for the inlet plane to the turbine.

The uniformity index (UI) is defined as

$$UI = \sum_i^n \sqrt{\left[\frac{[U_i - U_{Pi}]^2}{U_{Pi}^2} \right]} / n \quad (13)$$

where U_P is an approximation of a velocity profile com-

monly used for a fully developed turbulent pipe flow. A common expression form is:

$$U_P = V \cdot \left[1 - \frac{r}{R} \right]^{1/N} \quad (14)$$

Here we take $N=8$ and V is the maximum velocity. V is computed so that the mass flow at the inlet to the turbine is the same for the real case and the approximated velocity profile for the pipe flow.

In Figure 9 the secondary flow index and the uniformity index plotted versus time. As clearly seen, the deviation from a pure axial flow increases with increasing mass flow. It can also be noted that the different runners give different strength of secondary flow structures. The strongest secondary flow index is obtained for runners 1 and 4, which are the runners with the most curved bend upstream of the turbine inlet. These secondary flow structures, is a combinations of Dean vortices and swirling motion that are created in the bends of the manifold. The strength of these structures varies during the pulse. The near peak time in secondary flow index for runners 2 and 3 is broader as compared to runners 1 and 4. This aspect is due to the fact that these runners are shorter, which leads to less dissipation of secondary flow structures. The axial velocity profile deviates from a “pipe flow profile” due to the bends located upstream of the turbine, whereby one can observe higher axial velocity in the outer part of the bend outlet. As seen also in Figure 10, there are also regions with high velocity near the walls. Even though the differences in swirl and uniformity index for the four runners are not large, yet these indices correlate well with the instantaneous shaft power: i.e. runners which give the largest instantaneous index (runners 1 and 4) also gives the highest instantaneous shaft power. However, it is not enough to assess only the peak values of uniformity and swirl indices but one has to consider also the duration (or rather the integral of the index over time). It must also be emphasized that the mass flow, pressure and temperature trace (which give the available energy) are not the same for the four pulses assessed. Even though the efficiency curves are quite noisy, it seems that the highest efficiency is obtained for the mass flow pulses from runners 2 and 3, which are also the runners with the lowest peaks of the uniformity and secondary flow index.

The disturbances at the inlet to the turbine introduce viscous losses. One to give a measure of the losses is to compute a loss coefficient here defined as:

$$\frac{P_{Tot1} - P_{Tot2}}{P_{Tot1}} \quad (15)$$

where P_{Tot1} and P_{Tot2} are the total pressure at different evaluation plane.

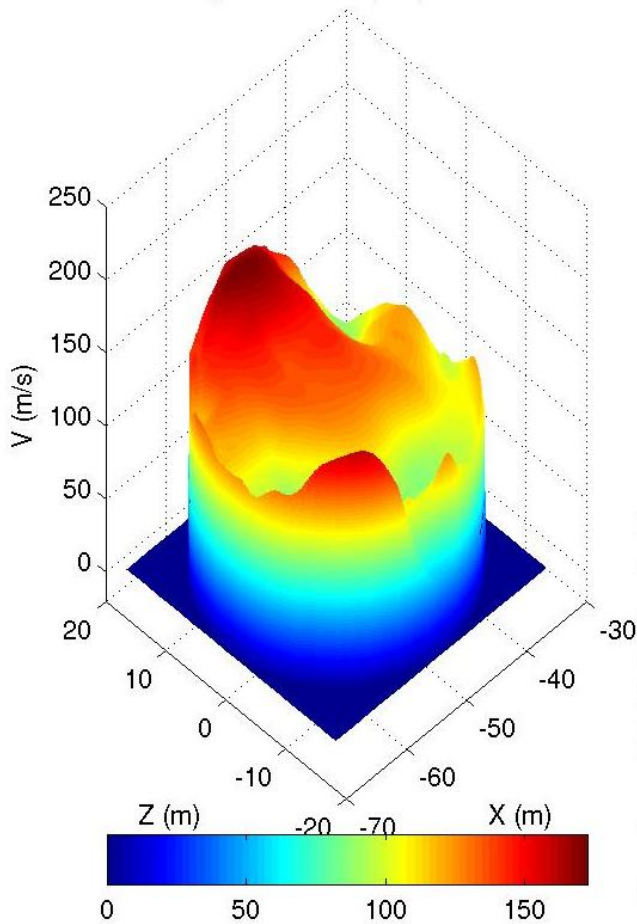


Figure 10. Surface plot of the axial velocity component at the inlet plane to the turbine at an instance with high mass flow.

The loss coefficient computed for a plane at the inlet to the turbine and the plane crossing the volute at the tongue is approximately 10%, when the mass flow through the turbine reaches its maximum. For the same instant, the loss coefficient for runner one (from the inlet to the runner and to the inlet to the turbine) is below 2%. In Figure 11, the total pressure in the complete turbine is plotted for an instance at high mass flow through the turbine, showing the high total pressure loss downstream of the inlet. This losses are due to the highly non-uniform axial velocity distribution at the inlet to the turbine and strong secondary flow structures, see Figure 13, which mainly are formed upstream of the turbine. When the mass flow through the turbine is high, the dissipation of the secondary flow structures is stronger, and hence the secondary flow structures in the volute become weaker. One of the main reasons to the very strong dissipation of the small scales in the secondary flow structures is the decreasing area from the inlet of the turbine to the smallest area at the tongue. This implies that the length scales of vortices decrease and since

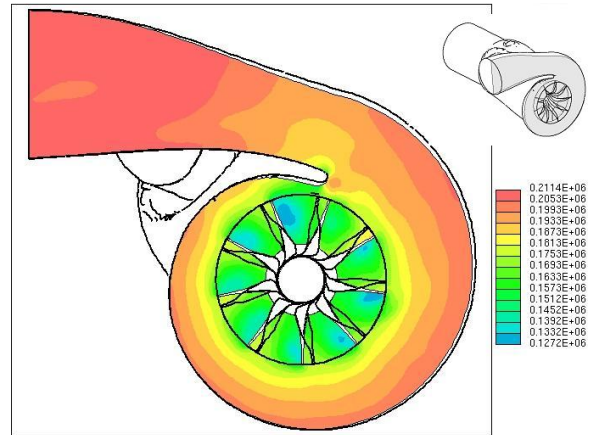


Figure 11. Total pressure at an instance of high mass flow through the turbine. The plane, shown in the small figure in the upper right corner, intersects the leading edge of the turbine blades in between the hub and shroud side.

the dissipation is inversely proportional to the length scale, the dissipation increases when the cross sectional area is decrease in the flow direction.

One way to visualize vortex cores is to use the λ_2 -technique [20]. The effects of the dissipation can be seen in the λ_2 plot, Figure 12, where almost no vortex cores is present in the volute for this instant. At this instant, the mass flow comes from runner 3, which also can be seen since there are a lot of different structures created in this runner. The back flow up into runners 1 and 4 can also be seen, since some structures are convected up in these runners. Downstream of the turbine, in the diffuser, a lot of both turbulent and coherent structures are created. At the outlet of the turbine, a strong swirling motion is the dominating secondary flow structure.

The axial velocity distribution in the volute becomes more uniform when the it is convected downstream, but still, far away from the most beneficial velocity distribution in the volute. The axial and secondary flow disturbances, in combination with the pulsatile flow, affect the relative incidence angle to the turbine wheel. For the operational point assessed in this study, the incidence angle varies from 60° to -90° during four pulses, which gives further incidence losses. At low mass flow rates, the relative incidence angle is less than -45° , which results in a weak vortex at the pressure side at the leading edge of the blades. When the mass flow is increasing, the relative incidence angle is increasing, and at high mass flow rates, the flow separates at the suction side of the leading edge. At high mass flow rate, the vortices created at leading edge are stronger than the vortices at low mass flow rates. These vortices created at the leading edge are convected down stream in the wheel, and at high mass flow rates, these vortices interacts with the blade tips vortices, and forming a strong structure with low axial velocity in the middle. The mech-

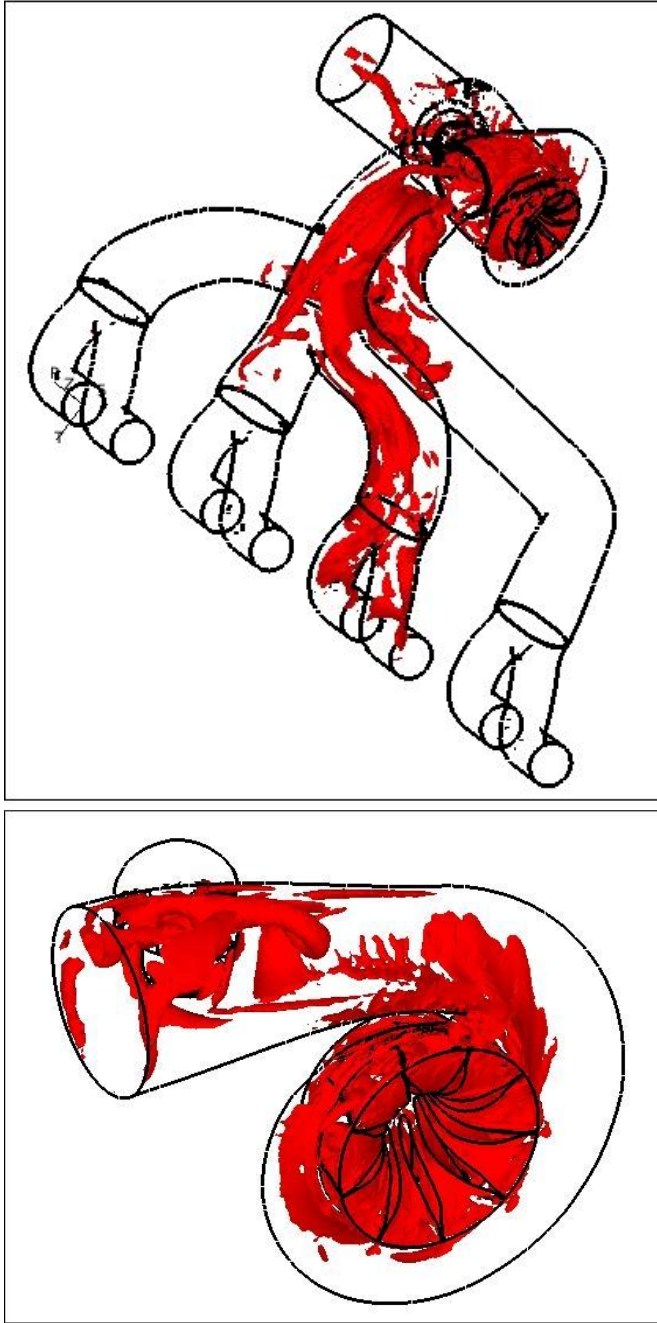


Figure 12. Vortex visualization with λ_2 at an instant with high mass flow from runner 3. Upper figure: The complete geometry. Lower figure: The volute and the wheel.

anism for these structures are the same as described in previous papers where both non-pulsatile and pulsatile flow in the same radial turbine were assessed ([5] and [17]). Even though the most of secondary flow structures have dissipated in the entrance

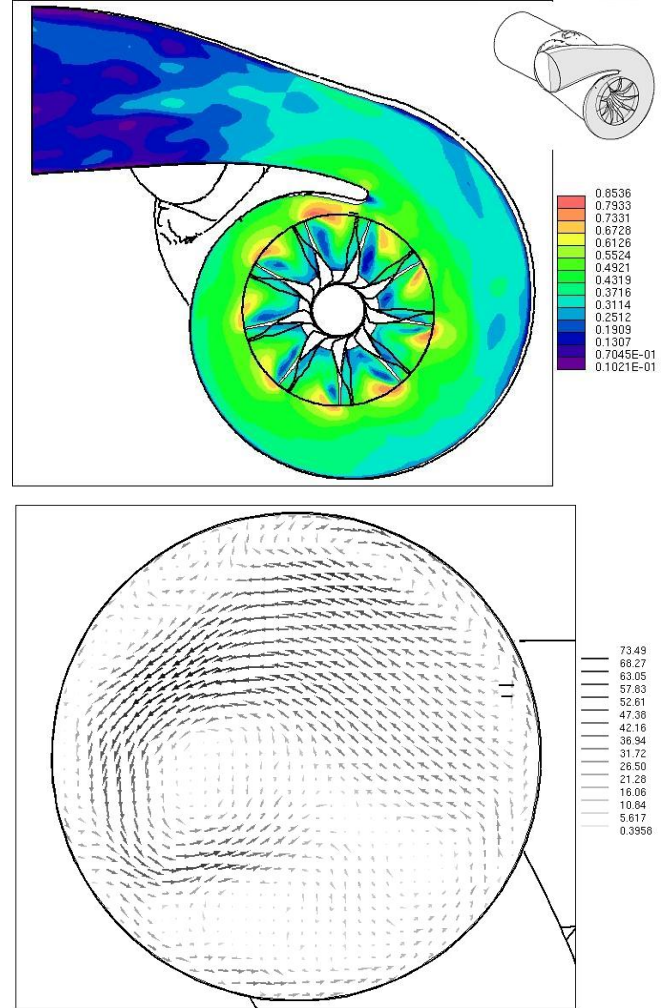


Figure 13. Snapshot of the velocity distribution at high mass flow rate. Upper figure: Contour plot of the Mach number in the volute and wheel. The plane, shown in the small figure in the upper right corner, intersects the leading edge of the turbine blades in between the hub and shroud side. Lower figure: Secondary flow at the inlet plane to the turbine.

region of the volute, the flow in the volute is still disturbed by a non-uniform in-plane motion at the inlet plane. For example, at some instants at high mass flow rates through the turbine, the flow separates at the shroud side of the inlet region to the wheel, see Figure 14. This results in a separation bubble, which affects the flow through the blade passage. This separation at the shroud side is due to high velocity at the wall region at the shroud side in the volute. This region of high velocity is an effect of the secondary flow at the inlet, which at this instant, consist of one strong vortex and several weaker vortex structures which are depicted in Figure 13.

Even though the flow field in the volute is disturbed, it does

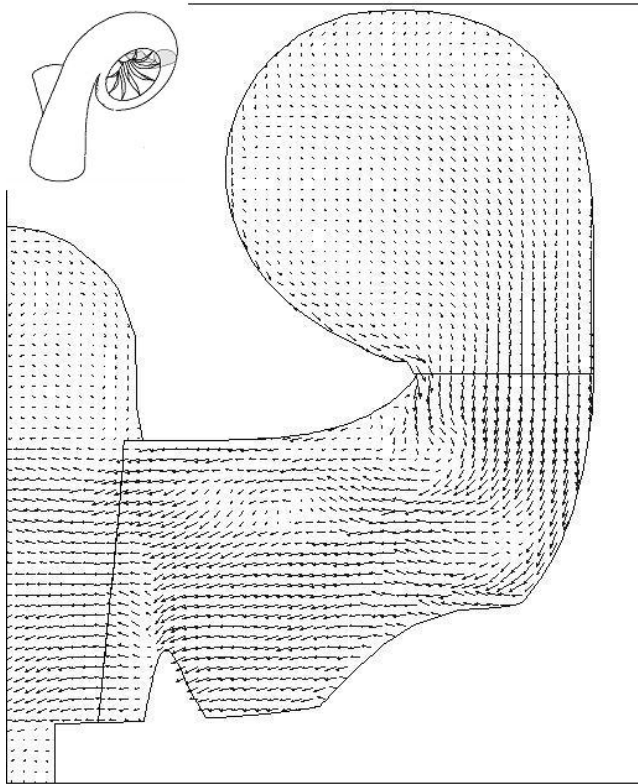


Figure 14. Velocity distribution in the volute and wheel at instant with high mass flow. The plotting plane is depicted in the small figure in the upper left corner.

not disturb the pressure distribution on the blades of the wheel in a severe way. On the pressure side, the pressure distribution is smooth, while one can see effects of separations zones and vortices created at the leading edge and over the blade on the pressure distribution at the suction side, which is depicted in Figure 15.

SUMMARY AND CONCLUSIONS

A Large Eddy Simulation of the flow field in an exhaust manifold and a radial turbine was conducted. At the inlet to the runner in the manifold a time resolved mass flow and temperature trace was applied. The amplitude and frequency of the mass flow and temperature corresponds to 4 cylinders two liters gasoline engine working at 1500 rpm.

As expected, the shaft torque varies in time due to the pulsatile flow. The shaft power is lower during the acceleration phase of the mass flow compared to deceleration phase, which form a closed loop when plotting the mass flow versus the shaft power. But, the shaft power is almost a linear function of the pressure at turbine inlet, which it was not for cases where a pul-

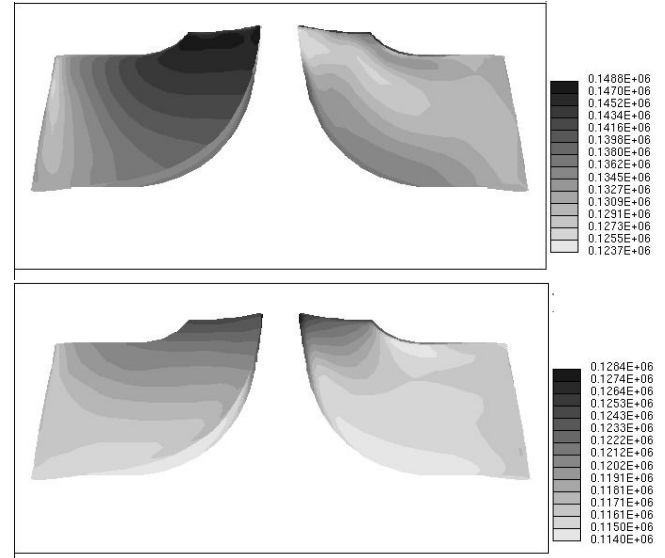


Figure 15. Pressure distribution at one blade. Right side: Pressure side, Left side: Suction side. Upper figure: At high mass flow. Lower figure: At low mass flow.

satile inflow condition was applied direct at the turbine. The geometry upstream of the turbine has a large effect on how the turbine behaves. The phase shift between the mass flow, pressure and shaft torque is below 4° , which is less than reported in the literature. This probably due to the effect of the manifold acting as a reservoir, which damps the pressure pulses and reduces the instantaneous mass flow through the turbine. The turbulence levels are also higher resulting in a lower phase shift. The small phase shift implies that a time resolved isentropic efficiency can be computed, and the instantaneous efficiency varies between approximately 0.1 and 1.1 during the pulses. A correlation between the strength of the disturbances of the inlet flow to the turbine and the isentropic efficiency was noted.

The results also show that the mass flow into the turbine is affected by the manifold. At instances when the peaks of the mass flow are expected, a substantial drop in the mass flow occurs, which is the results of back flow into the other runners. The pressure in the entire manifold varies almost in phase, and when the back flow is affected by the pressure gradient, it reverses and is convected down-stream in the turbine. The flow into the turbine is highly disturbed due to pulsatile flow and the geometrical configuration of the manifold. The axial velocity component shows a strong deviation from a uniform pipe flow profile and strong secondary flow structures are present. These disturbances are damped in the volute, causing a substantial pressure drop at high mass flow rates. Nevertheless, the flow in the volute is not uniform, which causes strong non-uniformity in the flow into the wheel. In the wheel, different secondary flow structures and separation zones are present. However, this only seems to affect

the pressure distribution on the suction side of the blades. At the pressure side, the pressure distribution is smooth at both high and low mass flow rates.

Since the flow field is highly unsteady and turbulent, it is not straightforward to determine the mechanism of the different types of losses for this case. The complexity of the flow due to the geometry has to be reduced, which can be done by assess the effects of pulsatile flow using different bent pipe configurations upstream of the turbine.

ACKNOWLEDGMENT

The work was sponsored by the Swedish Emission Research Program, EMFO and GM Powertrain, Sweden. Thanks are also due to the computer centers at KTH (PDC) and LiU (NSC) for the provided computer resources required to carry out this work.

REFERENCES

- [1] Winterbone, D. E., Nikpour, B., and Alexander, G. I., 1990. "Measurements of the performance of a radial inflow turbine in conditional steady and unsteady flow". *ImechE Conference Transactions, 4th International Conference: Turbocharging and turbocharging*, **C405/015**, pp. 153–160.
- [2] Winterbone, D. E., Nikpour, B., and Frost, H., 1991. "A contribution to the understanding of turbocharger turbine performance in pulsating flow". *International Conference on Internal Combustion Research, Paper no C433/011. Inst. of Mech. Engrs.*, pp. 19–28.
- [3] Dale, A., and Watson, N., 1986. "Vaneless radial turbocharger turbine performance.". *ImechE Conference Transactions; "Turbochargers and Turbocharging"*, London, pp. 65–76.
- [4] Capobianco, M., and Gambarotta, A., 1990. "Unsteady flow performance of turbocharger radial turbines". *C405/017, Proceeding of the Institute of Mechanical Engineers, Fourth International Conference, Turbocharging and Turbochargers*, pp. 123–132.
- [5] Hellstrom, F., and Fuchs, L., 2008. "Numerical computations of pulsatile flow in a turbo-charger". *AIAA-2008-073, 46th AIAA Aerospace Sciences Meeting and Exhibit, Reno, Nevada, 7-10 January 2008*.
- [6] Wallace, F., Adgey, J., and Blari, G., 1969. "Performance of inward radial flow turbines under non-steady flow conditions". *Proc Instn Mech Engrs*, **184**, pp. 183–195.
- [7] Benson, R., and Scrimshaw, K., 1965. "An experimental investigation of non-steady flow in a radial gas turbine.". *Instn Mech Engrs*, **180**, pp. 74–85.
- [8] Karamanis, N., Martinez-Botas, R., and Su, C., 2001. "Mixed flow turbines: Inlet and exit flow under steady and pulsating conditions". *ASME Journal of Turbomachinery*, **123**, pp. 359–371.
- [9] Arcoumanis, C., Karamanis, N., Martinez-Botas, R., and Su, C. C., 1999. "Unsteady characteristics of a mixed-flow turbocharger turbine". *IMechE paper no C557/030*, pp. 905–921.
- [10] Lam, J. K. W., Roberts, Q. D. H., and McDonnell, G. T., 2002. "Flow modelling of a turbocharger turbine under pulsating flow". *ImechE Conference Transactions from 7th International Conference on Turbochargers and Turbocharging, 14-15 May London UK*, pp. 181–196.
- [11] Palfreyman, D., and Martinez-Botas, R., 2005. "The pulsating flow field in a mixed flow turbocharger turbine: An experimental and computational study". *ASME, Journal of Turbomachinery*, **127**, pp. 144–155.
- [12] Wendt, G., Mickan, R., Kramer, R., and Dopheide, D., 1996. "Systematic investigation of pipe flows and installation effects using laser doppler anemometry- part 1. profile measurements downstream of several pipe configurations and flow conditioners.". *Flow Measurements and Instrumentations*, **7**, pp. 141–149.
- [13] Mickan, R., Wendt, G., Kramer, R., and Dopheide, D., 1996. "Systematic investigation of pipe flows and installation effects using laser doppler anemometry- part ii. the effect of disturbed flow profiles on turbine gas meters-a describing empirical model". *Flow Measurements and Instrumentations*, **7**, pp. 151–160.
- [14] Hellstrom, F., and Fuchs, L., 2007. "Numerical computations of steady and unsteady flow in bended pipes.". *AIAA-2007-4350, 37th AIAA Fluid Dynamics Conference and Exhibit, Miami, FL, June 25-28*.
- [15] Erlich, D. A., Lawless, P. B., and Fleeter, S., 1997. "Particle image velocimetry characterization of a turbocharger turbine inlet flow". *SAE Paper 971565, 48th SAE Earth-moving Industry Conference and Exposition, Peoria, IL*, pp. 121–127.
- [16] Steenbergen, W., and Voskamp, J., 1998. "The rate of decay of swirl in turbulent pipe flow". *Flow Measurements and Instrumentations*, **9**, pp. 67–78.
- [17] Hellstrom, F., and Fuchs, L., 2008. "Effects of inlet conditions on the turbine performance of a radial turbine". *GT 2008-51088, ASME Turbo Expo 2008, Power for Land, Sea and Air, Berlin, Germany*.
- [18] Celik, I. B., 2005. "Procedure for estimation and reporting of discretization error in cfd applications". *Internal report, Mechanical and Aerospace Engineering Department, West Virginia University, Morgantown Wv, USA, is-mail.celik@mail.wvu.edu*.
- [19] Flaxington, A., and Swain, E., 1999. "Turbocharger aerodynamic design". *Proceedings of the Institute of Mechanical Engineers, Vol 213 Part C*, pp. 43–57.
- [20] Jeong, J., and Hussain, F., 1995. "On the identification of a vortex". *Journal of Fluid Mechanics*, **285**, pp. 69–94.